

Cite this: *J. Mater. Chem. A*, 2020, **8**, 2654

## Advanced hermetic encapsulation of perovskite solar cells: the route to commercialization†

Seyedali Emami,<sup>1</sup> Jorge Martins,<sup>1</sup> Dzmitry Ivanou<sup>1</sup> and Adélio Mendes<sup>1\*</sup>

Though perovskite solar cells (PSCs) are rapidly emerging into the photovoltaic (PV) community, their long-term stability raises huge concerns for their future commercialization. PSCs are sensitive to humidity and temperature. A hermetic encapsulation is crucial for PSCs not only to prevent them from external environmental effects but also to avoid leakage of Pb-containing materials of the cells. An advanced laser-assisted glass-frit encapsulation method is developed to seal HTM-free PSCs. The long-term stabilities of the laser-sealed devices are examined under harsh environmental conditions of humidity and temperature exposure tests. The hermetically sealed PSCs have passed 70 thermal cycles (−40 °C to 85 °C) and 50 h damp heat (85 °C, 85% RH) tests according to the IEC61646 standard. The power conversion efficiency of hermetically encapsulated PSCs remained constant for 500 h under humid air feeding exposure (80 ± 5% RH); non-hermetically encapsulated devices degraded after ca. 50 h. This work indicates that the hermeticity level of an encapsulation plays a key role in the stability of the devices in a humid environment. Therefore, a hermetic encapsulation is vital for the industrialization of PSCs.

Received 29th October 2019  
Accepted 2nd January 2020

DOI: 10.1039/c9ta11907h

rsc.li/materials-a

### Introduction

Perovskite solar cells (PSCs) were first reported in 2009 by Kojima *et al.*<sup>1</sup> with power conversion efficiency (PCE) of 3.8%. In only 10 years their PCEs have reached values as high as 25.2% for a single junction and 28% in monolithic tandem with silicon.<sup>2</sup> To date, most of the research effort has been intensely focused on achieving high PCEs and little attention has been paid to long-term stability. High PCEs and a simple fabrication method allow perovskite solar cells to be a strong candidate for entering the photovoltaic (PV) market. However, the future commercialization of PSCs relies on long-term stability assurance. Most of the long-term stability research is dedicated to perovskite materials and device structure modifications neglecting PSC encapsulation. Here, we show the crucial importance of hermetic encapsulation for the long-term stability of PSCs.

The most common instability sources of PSCs are temperature and humidity.<sup>3</sup> To pass the requirements of the common PV standard tests such as IEC61646, PSCs must be stable at the temperature range of −40 °C to 85 °C and relative humidity of 85%.<sup>4</sup> Therefore, the device should be fabricated with thermally stable materials and properly sealed to avoid humidity and moisture related issues. The thermal stability of PSCs depends

on the device structure. Common PSCs include an electron transport layer (ETL), a mesoporous scaffold, a perovskite absorber, a hole transport material (HTM) and a back contact. While most ETLs and scaffolds are thermally stable, perovskite absorbers and HTMs decompose at elevated temperatures.<sup>5</sup> Perovskite absorbers are commonly synthesized using cations such as methylammonium (MA), formamidinium (FA) and Cs along with Pb. The most widely used MAPbI<sub>3</sub> is stable up to 120 °C,<sup>6</sup> while FAPbI<sub>3</sub> and Cs<sub>0.10</sub>FA<sub>0.90</sub>Pb(I<sub>0.83</sub>Br<sub>0.17</sub>)<sub>3</sub> display better thermal stability.<sup>7,8</sup> Nevertheless, all of the aforementioned perovskites are thermally stable at 85 °C; hence they would pass the requirements of the IEC standard. In contrast, widely used organic HTMs such as spiro-OMeTAD (2,2',7,7'-tetrakis(*N,N*-di-*p*-methoxyphenyl)-amine) 9,9' spirobifluorene) decompose at ca. 70 °C.<sup>9</sup> Other HTMs such as PTAA (poly(*tri*-arylamine)), CuSCN (copper(I) thiocyanate) and CuPc (copper phthalocyanine) show thermal stability at 85 °C.<sup>8,10–12</sup> In this context, HTM is the most vulnerable part of the device for passing industry related standards.

Since perovskite materials are capable of transporting both electrons and holes,<sup>13</sup> PSCs can be fabricated without the HTM layer.<sup>14,15</sup> HTM-free structures are a promising candidate for commercialization of PSCs due to their simple air processed fabrication. These devices are fabricated by the infiltration of a perovskite crystal precursor into screen printed mesoporous stacked layers of TiO<sub>2</sub> scaffold/insulation layer (*e.g.* ZrO<sub>2</sub>, Al<sub>2</sub>O<sub>3</sub>)/ back contact (*e.g.* Au, C). A fully screen printed HTM-free mesoscopic TiO<sub>2</sub>/ZrO<sub>2</sub>/C device with a mixed cation perovskite of 5-ammoniumvaleric acid (5-AVA) and MA reached a certified

LEPABE – Laboratory for Process Engineering, Environment, Biotechnology and Energy, Faculdade de Engenharia, Universidade do Porto, Rua Dr Roberto Frias, 4200-465 Porto, Portugal. E-mail: mendes@fe.up.pt

† Electronic supplementary information (ESI) available. See DOI: 10.1039/c9ta11907h

PCE of 12.8% and 1000 h stability in ambient air.<sup>16</sup> The hydrophobic carbon back contact in this structure improves the stability issues of the cell in a humid environment, while lack of an HTM makes the devices stable up to the thermal stability of the perovskite absorber (*i.e.* above 85 °C). A study by Grätzel *et al.* showed that the performance of HTM-free PSCs can be even further improved through humidity and thermal exposure (HTE) treatment.<sup>17</sup> They showed that *ca.* 115 h of 70 ± 5% RH at 40 °C treatment of the cells would assist the crystal growth of perovskite at the TiO<sub>2</sub> scaffold.<sup>17</sup> The hydrophobic carbon back contact acts as a blocking mesh to avoid penetration of liquid water while permitting diffusion of water vapor through ZrO<sub>2</sub> to assist the irreversible (5-AVA)<sub>0.05</sub>(MA)<sub>0.95</sub>PbI<sub>3</sub> crystal growth not only in TiO<sub>2</sub> but also in the entire mesoporous media.<sup>17</sup>

Although intense effort is being made by many researchers for developing PSCs stable in humid environments, successful commercialization of these PV devices requires encapsulation. Thus, encapsulation plays a key role in the transition of PSCs from laboratory scale devices to real outdoor commercial panels. In this context, a suitable airtight encapsulation can be used to avoid humidity and oxygen exposure of the PSCs, regardless of the device structure. There are three levels of hermeticity for an encapsulation: (i) gross leak, (ii) non-hermetic and (iii) hermetic. The gross leak test is commonly performed by tracing liquid penetration into the cavity of an encapsulated sample immersed in a liquid (*e.g.* dye). A sample with no gross leakage must be further examined with a gas (*e.g.* helium) for fine leaks. According to the MIL-STD-883 standard, a sealing with helium leak rate lower than  $5 \times 10^{-8}$  atm cm<sup>3</sup> s<sup>-1</sup> is considered as hermetic.<sup>18</sup>

In addition, the long-term stability of a hermetic sealing must be examined by simulated climatic tests to ensure >20 years lifetime of the encapsulation. The long-term stability of the sealing is commonly studied by environmental cycling tests as described in IEC61646.<sup>4</sup> These tests include:

- Thermal cycle test: -40 °C to 85 °C (no RH control);
- Damp heat test: 85 °C and 85% RH.

The long-term stability of an encapsulation is, perhaps, even more critical than its initial hermeticity. Though several sealants display hermeticity initially, few of them can retain their hermeticity after stability tests.<sup>19</sup>

To date, various sealants and sealing methods have been used for PSCs. The sealing method can be divided into two major categories: (i) thin film in which a thin protective layer is deposited on top of the cell;<sup>20</sup> (ii) edge seal in which the sealant is placed around the cell and it is bonded to a cover substrate.<sup>21</sup> For the thin film encapsulation method, the coefficient of thermal expansion (CTE) of the protective layer should be close to the components of the cell, to avoid mechanical damage during stability tests.<sup>22</sup> In contrast, the edge seal method is more reliable for stability tests; however, this method commonly requires additional thermal or light curing steps; therefore, the additional curing step should not affect the performance of the device.

The most widely used edge sealants for PSCs are epoxy resin and thermoplastics. UV illumination can degrade perovskite solar cells containing a TiO<sub>2</sub> layer.<sup>23</sup> Thus for UV curing of epoxy

resin the active area must be masked to avoid performance losses in the device.<sup>21</sup> In the case of thermal curing epoxy sealants, the heating step can cause contamination to the cell due to outgassing of the epoxy.<sup>24</sup> Thermoplastic bonding is commonly achieved at *ca.* 140 °C in 10 min to 20 min under an applied mechanical force. In this context, sealants such as EVA (ethylene vinyl acetate)<sup>22</sup> and a combination of polyolefin “ENLIGHT” with butyl rubber<sup>25</sup> display superior performance after thermal and damp heat stability tests.

Glass frit encapsulation is an alternative edge sealant to thermoplastic sealing. While common thermoplastics are neither hermetic nor long-term stable, glass frit encapsulation displays a unique hermeticity even after stability tests according to IEC61646.<sup>19</sup> Similar to thermoplastics, glass frit bonding is achieved through thermal treatment. Most glass frits have a bonding temperature above 380 °C; higher than the thermal decomposition of the perovskite solar cells. To decrease the process temperature of the encapsulation a laser-assisted sealing method can be used. This method uses a laser beam to locally heat up the sealant material to its melting point while the device is kept at a lower process temperature.

Laser-assisted material processing has been widely used for various industrial solutions. One of the highlighted advantages of laser-processing is its localized material processing feature. Therefore, for laser-assisted encapsulation of solar cells, the active area of the device is not required to be masked for avoiding performance losses due to sealant processing. Laser-assisted glass frit encapsulation for solar cells was first reported in 2012 by Mendes *et al.* for dye-sensitized solar cells (DSCs).<sup>26</sup> A detailed description of a laser-assisted sealing method can be found elsewhere.<sup>19,26,27</sup> Briefly, the laser-sealing apparatus consists of three major components: (i) a heating source (*e.g.* hot plate or furnace) to heat up the specimen to the process temperature; (ii) a laser source to deliver the heat required to locally melt/bond the sealant; and (iii) laser radiation optic elements to control the emission velocity and beam focusing during the encapsulation process. During laser radiation, the temperature at the sealing line must rise to values slightly above the bonding temperature of the glass frit to achieve the sealing. This happens in a matter of few dozens of milliseconds and the external heating source assists the encapsulation process by lowering the thermal gradient on the substrate.

Glass frit encapsulation relies on the CTE match of the frit and substrates. For PSC application the substrates are made of a transparent conductive oxide (TCO) coated soda-lime glass substrate with a CTE of *ca.*  $9 \times 10^{-6}$  K<sup>-1</sup>; therefore the CTE of the glass frits must be close to this range.

During the laser processing, the minimum Laser-Added (LA) temperature difference required to achieve sealing is the difference between the bonding point of the sealant (*i.e.* glass frit) and laser-assisted process temperature:

$$\Delta T_{LA, \text{minimum}} = T_{\text{bonding}} - T_{\text{process}} \quad (1)$$

To achieve high quality bonding with no delamination and cracks,  $\Delta T_{LA}$  should not surpass the thermal shock resistance of

the encapsulation configuration (Fig. 1). The thermal shock resistance of a material depends on various properties such as CTE, thermal diffusivity, elastic modulus, tensile strength, thermal conductivity, fracture toughness, heat transfer coefficient, sample size and thermal shock duration.<sup>28</sup> The encapsulation configuration comprises substrates and sealants. Since the thermal shock resistance of the substrates is limited to the properties of the soda-lime glass, the properties of the glass frit materials determine the overall resistance of an encapsulation configuration. The laser-assisted sealing method mechanism is based on the laser beam radiation absorbance of the glass frits. Since the glass substrate is transparent at the laser emission wavelength, the glass frits are the main heat transfer media of the encapsulation configuration. Therefore, the thermal conductivity of glass frits defines the thermal shock resistance of the encapsulation configuration. Glass frits with higher thermal conductivity would provide higher thermal shock resistance to the sealing configuration.

Common glass frit compositions include oxide materials such as SiO<sub>2</sub>, B<sub>2</sub>O<sub>3</sub>, Bi<sub>2</sub>O<sub>3</sub>, ZnO, V<sub>2</sub>O<sub>5</sub> and PbO. The parameters with more influence on the sealing process temperature are the bonding temperature and the thermal conductivity of the glass frits. A possible strategy for increasing the thermal conductivity of glass frits is to add silver nanoparticles to their composition. However, adding Ag to the frit would lead to electrical conductivity along the sealant.

Laser-assisted glass frit sealing can produce long-term stable hermetic encapsulation.<sup>19,27</sup> Moreover, the glass frit laser-sealing process can be applied to encapsulate large devices.<sup>27</sup> Therefore, this process can provide a scalable hermetic encapsulation for PSC application. A desired laser-assisted sealing for PSC application should be electrically insulating and should display a process temperature below 140 °C.

The previously reported room temperature laser sealed encapsulation with Ag based glass frits was not compatible for PSC applications due to its electrical conductivity.<sup>19</sup> We have

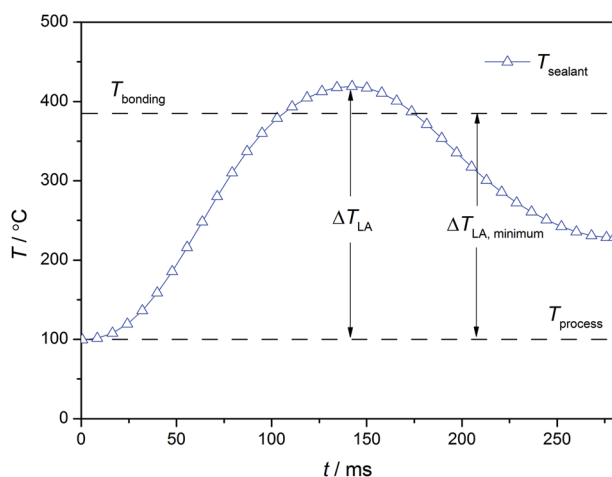


Fig. 1 Experimental temperature history of  $T_{\text{sealant}}$  (on the sealant) during a laser-assisted sealing process for a  $T_{\text{process}}$  (i.e. device temperature) and  $T_{\text{bonding}}$  (melting/bonding temperature of the sealant) of 100 °C and 380 °C, respectively.

recently reported a laser-assisted glass frit encapsulation method at 120 °C process temperature.<sup>27</sup> In the present work, several glass frit materials were studied to further decrease the sealing process temperature to 100 °C. Decreasing the process temperature requires not only a detailed study of glass frit material properties but also re-optimization of laser emission parameters.

To date, the most effective encapsulation method reported is by McGehee *et al.* in which the authors used a relatively wide sealant material (15 mm); therefore, current collectors were required for charge collection.<sup>25</sup> An industrially compatible encapsulation solution for PSCs must not affect the performance of the cells and should be as narrow as possible to minimize the cost. Here we report a laser-assisted glass frit encapsulation method of HTM-free PSCs at a process temperature of *ca.* 100 °C. This scalable encapsulation method is compatible with the fabrication process of PSCs and does not require additional current collectors. The current process temperature is compatible with HTM-free PSCs while it can also be applied to any other PSC device configuration such as conventional HTM-based or inverted cells with superior thermal stability.

## Materials and methods

### Device fabrication

HTM-free devices were fabricated by the sequential screen print deposition of mesoporous layers of TiO<sub>2</sub>, ZrO<sub>2</sub> and carbon back contact. The perovskite absorber is then infiltrated into the mesoporous structure by dropcasting the precursor solution on top of the carbon layer. Similar to TiO<sub>2</sub>, ZrO<sub>2</sub> and C, glass frits are also required to be sintered after screen printing. Therefore, the sintering steps of the glass frits and components of the device must be compatible to avoid thermal degradation of both sealant and the cell components.

The substrates (TEC 7 from Greatcell Solar) were ultrasonically washed in distilled water and detergent. After drying, the substrates were further cleaned with UV-O<sub>3</sub> for 20 min. Then, a precursor solution of titanium diisopropoxide bis(acetylacetonate) in anhydrous 2-propanol was used to deposit a compact TiO<sub>2</sub> blocking-layer by spray pyrolysis at 450 °C. Afterwards, a 2 × 2.5 cm<sup>2</sup> rectangular shape with 4 mm linewidth of glass frit A was screen-printed and sintered at 500 °C. Then, the mesoporous layers of TiO<sub>2</sub> (T165/SP from Solaronix) and ZrO<sub>2</sub> (ZT/SP from Solaronix) were screen-printed and annealed at 500 °C, respectively. Afterwards, a 2 × 2.5 cm<sup>2</sup> rectangular shape with 1 mm linewidth of glass frit B was screen-printed and sintered at 400 °C. Then, the carbon back contact (Elcocarb B/SP from Solaronix) was screen-printed and sintered at 400 °C. Finally, 5 μl of (5-AVA)<sub>0.05</sub>(MA)<sub>0.95</sub>PbI<sub>3</sub> in GBL precursor solution (from Solaronix) was dripped on top of the mesoporous structure and sintered at 70 °C. The cover glass substrate was cleaned as described for cell substrates, before screen-printing and 450 °C sintering of a 2 × 2.5 cm<sup>2</sup> rectangular shape with 1 mm linewidth of glass frit C. For large area devices, the glass frit size and precursor solution volume were 4 × 4 cm<sup>2</sup> and 20 μl, respectively. The entire device fabrication process was performed under atmospheric conditions with an RH range of 40% to 60%.

Devices were subjected to humidity and thermal exposure (HTE) to improve their performance. A saturated salt solution environment was used for HTE treatment before encapsulation. Treatment was carried out by placing the cells inside a desiccator filled with a saturated solution of NaCl to achieve *ca.* 70% RH at 40 °C inside a furnace, Fig. S1a (ESI†).

HTM-based devices were fabricated according to procedures described elsewhere.<sup>8,10</sup>

### Glass frit properties and configuration

As mentioned before, the composition of the glass frit defines its thermal conductivity and its thermal shock resistance during the laser-assisted sealing process. A simplified method was used to compare the thermal conductivity of glass frits, Fig. S2 (ESI†). Tables S1 and S2 (ESI†) present the properties of several studied glass frits and their laser-assisted sealing conditions. To achieve an encapsulation configuration with suitable thermal conductivity, a multi-layer glass frit sealant configuration was used for encapsulation. Table 1 shows the characteristics of the glass frits used for the present work. Glass frits A and B were sequentially deposited on the device substrate while glass frit C was deposited on the cover glass substrate. Therefore, the laser-assisted bonding was achieved through sealing glass frit B to glass frit C. The thicknesses of screen printed glass frits after sintering are *ca.* 17 μm, 22 μm and 13 μm for glass frits A, B and C, respectively. The total thickness of the encapsulation after the laser-sealing process is *ca.* 52 μm.

It is worth mentioning that glass frits B and C can be laser-sealed at a process temperature of 120 °C.<sup>27</sup> However, to decrease the process temperature, glass frit A was added to increase the overall thermal conductivity of the encapsulation configuration. Fig. 2 illustrates the schematic view of glass frit configurations and the PSC device structure.

During the laser-sealing process, the laser beam is radiated through the cover glass; therefore, the temperature required to achieve the bonding is the bonding temperature of glass frit B to melt and seal to glass frit C. Each of the triple layer glass frit plays a different role; glass frit C, with the highest thermal conductivity, can withstand rapid thermal stress due to direct radiation of the laser beam; glass frit B has the lowest melting point to minimize the bonding temperature; finally, glass frit A acts as the thermal shock absorbing layer. The width of the screen printed sealing line for glass frits B and C is 1 mm. The heat affected zone (HAZ) during the laser emission is *ca.* 2 mm.<sup>19</sup> Therefore, during the laser process the temperature at the sealing line reaches values slightly higher than 380 °C, while 2 mm away from the sealing line the temperature at the

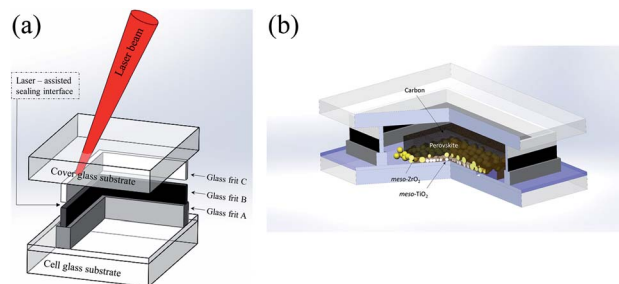


Fig. 2 Schematic view of (a) the triple layer glass frit laser-assisted sealing configuration, and (b) encapsulated HTM-free PSC device.

substrates is equal to the process temperature. Thus, to maximize the advantage of better thermal conductivity of glass frit A, this frit was deposited with 4 mm width – Fig. 2a.

### Laser-assisted encapsulation

The laser-assisted sealing process was performed with an in-house apparatus described elsewhere.<sup>19</sup> Briefly, the apparatus consists of a continuous wave laser source ( $\lambda = 1070$  nm), a 2D galvanometer scan head, an f-theta lens, and a hot plate to provide the processing temperature during the laser-sealing process. The laser-assisted encapsulation process was carried out by heating the cells to the desired sealing process temperature for various dwell times. The design of experiments methodology was used to optimize the effect of the encapsulation process on the performance of the PSC device. The optimal laser-sealing conditions were: 41 W power and 210 mm s<sup>-1</sup> scanning velocity at *ca.* 0.6 mm spot size.

### Hermeticity test of the encapsulated device

The hermeticity of the optimized encapsulation method was measured according to the MIL-STD-883 standard.<sup>18</sup> A previous study<sup>27</sup> showed that this test method is only valid for devices with an internal cavity area <5.5 × 5.5 cm<sup>2</sup>. The cavity areas of the cells for the present work are 2 × 2.5 cm<sup>2</sup> and 4 × 4 cm<sup>2</sup>; therefore, the MIL-STD standard is valid. The leak rates of the encapsulated packages were measured according to method 1014.13, A2. For method A2 the leak rates must be reported in the equivalent air leak rate (*L*). The equivalent air leak rate (*L*) rejection limit for the encapsulation under study is 1 × 10<sup>-7</sup> atm cm<sup>3</sup> s<sup>-1</sup>. Air leak rates higher than 1 × 10<sup>-5</sup> atm cm<sup>3</sup> s<sup>-1</sup> Air are considered as gross leakages. The test conditions for a fine helium leak rate were 5 h of He bombing at 2 bar. More details on the leak rate measurement method can be found elsewhere.<sup>27</sup>

### Long-term stability tests

Climatic tests according to IEC61646 were performed in an industrial climatic chamber (Fitoclima from Aralab). Fig. S3 (ESI†) shows the temperature and humidity history for the climatic tests. The humid air feed was produced by humidifying a 450 mL min<sup>-1</sup> dry air feed to a cylindrical column filled with distilled water. The humid air was then fed to a 17.5 × 17.5 × 6

Table 1 Properties of glass frit materials

Glass frit	Composition	CTE × 10 <sup>-6</sup> /K <sup>-1</sup>	Bonding temperature/ °C
A	SiO <sub>2</sub> ·B <sub>2</sub> O <sub>3</sub> ·PbO	7.8	430
B	TeO <sub>2</sub> ·V <sub>2</sub> O <sub>5</sub>	8.4	380
C	BaO·SiO <sub>2</sub> ·PbO·Ag	9.0	450

$\text{cm}^3$  stainless steel chamber where the devices were stored. The temperature of the chamber was kept constant using a hotplate, and the humidity level was monitored with a humidity sensor. Fig. S1b (ESI†) shows the scheme of the humid air exposure chamber apparatus. Three groups of devices (with different hermeticity levels) were tested for humid air feeding exposure: no sealing, non-hermetic sealing and hermetic sealing. The quality of the laser-sealed devices depends on the laser emission power and scanning velocity. Usually, optimized laser conditions produce a high quality crack-free sealing; however, in some cases the final sealing may include defects such as cracks and delamination. If a device with minor defects on the sealing passes a gross leak test, its hermeticity would be categorized as non-hermetic.

### Characterization

The current–voltage ( $J$ – $V$ ) curves were recorded using an electrochemical workstation (Zahner Zennium) under AM1.5 illumination of  $100 \text{ mW cm}^{-2}$  using an Oriel class ABA LED solar simulator (MiniSol LSH 732 from Newport). The illumination light was calibrated with a Si reference cell. The scan rate for  $J$ – $V$  curves was  $4 \text{ mV s}^{-1}$  and the masked devices (*ca.*  $0.2 \text{ cm}^2$  and  $1 \text{ cm}^2$  mask area for small and large device sizes, respectively) were soaked with light for *ca.* 60 s before measurements. The reflectance spectra of the cells were measured with a UV-VIS-NIR spectrophotometer (Shimadzu UV-3600). The incident photon to current conversion efficiency spectra were recorded without biased light illumination using a semi-automatic station (Newport). The XRD spectra were collected on a Philips X'Pert MPD diffractometer (Cu  $K\alpha$  radiation). The SEM images of the glass frit sealing were acquired with a benchtop microscope (Phenom XL).

## Results and discussion

### Encapsulation optimization

The process temperature and dwell time of the laser-assisted sealing procedure can affect the performance of the PSC devices. Therefore, a response surface methodology (RSM) model with two-factor variables (sealing process temperature and heating dwell time) and three-factor response (sealing quality, sealing reproducibility and sealing process effect on the performance of the PSC device) were considered, to minimize the mentioned effect. Table S3 (ESI†) shows the factors of the model; the intervals for sealing process temperature and heating dwell time were  $80 \text{ }^\circ\text{C} < T < 120 \text{ }^\circ\text{C}$  and  $20 \text{ min} < t < 60 \text{ min}$ , respectively. The response interval range was 0 to 10. For sealing quality, the response was rated based on the visual inspection of the encapsulation after laser processing. For sealing reproducibility, the response was based on the reproducibility of the sealing experiments. Finally, the sealing procedure effect on the PSC performance was ranked by analyzing the photovoltaic parameters of the cell before and after the encapsulation. Design expert 10 software was used for fitting the responses of the model. Table S4 and Fig. S4 (ESI†) show the predicted response functions and their contour plots.

To optimize the multi-response process, the desirability function was applied to the three responses of the RSM model. The weight factors of the response for the desirability function of the sealing effect on the PSC, sealing quality and reproducibility were 0.5, 0.375 and 0.125, respectively. Therefore, the goal was set to minimize the performance loss of the cell and achieve high quality encapsulation with a reasonable reproducibility rate.

As shown in Fig. 3, the highest desirability conditions can be achieved at  $95 \text{ }^\circ\text{C} < T < 105 \text{ }^\circ\text{C}$  and  $25 \text{ min} < t < 40 \text{ min}$ . The optimal condition is for *ca.*  $T = 100 \text{ }^\circ\text{C}$  and  $t = 35 \text{ min}$  with a desirability value of 0.82.

HTM-free fully printable PSCs were used for the current study, due to their simple air processed fabrication method and their potential for commercialization. Therefore, the optimal conditions of the RSM model are mostly valid for HTM-free devices with  $\text{TiO}_2/\text{ZrO}_2/\text{C}$  and  $(5\text{-AVA})_{0.05}(\text{MA})_{0.95}\text{PbI}_3$  perovskite absorber. As shown in Fig. S4 (ESI†) the highest encapsulation quality and reproducibility response are achieved at higher process temperatures and dwell times, while the negative effect on the HTM-free PSC is more pronounced at temperatures higher than *ca.*  $105 \text{ }^\circ\text{C}$ .

As mentioned, humidity and thermal exposure (HTE) improve the performance of HTM-free PSCs. Fig. S5 and S6 (ESI†) demonstrate the effect of HTE on the performance of the devices. While there was no change in the  $V_{oc}$  after the HTE treatment, a notable increase in the  $J_{sc}$  and PCE of the devices was achieved. For FF the results indicate a decrease after the HTE; however, since the  $J$ – $V$  curves of fresh cells have a so-called “bump” (Fig. S6†), the FF values for these cells should contain false positive errors while after HTE the results contain no such error. After the HTE treatments, the cells were sealed according to the optimal conditions of the RSM model. As shown in the  $J$ – $V$  curves of Fig. S6 (ESI†), the performance of the device remained unchanged after the encapsulation process. Fig. 4 presents the statistics for the photovoltaic parameters ( $V_{oc}$ ,  $J_{sc}$ , FF and PCE) of the tested devices before and after sealing.

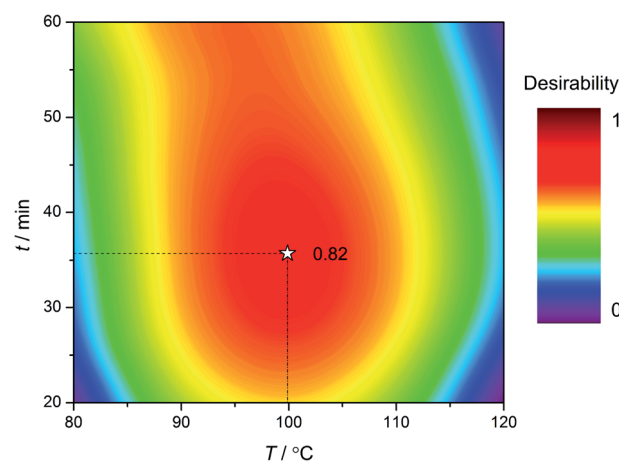


Fig. 3 Contour plot of the desirability function of the responses for the RSM model to optimize the encapsulation procedure.

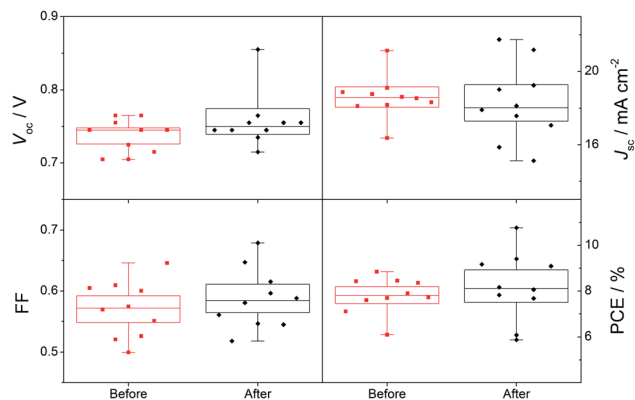


Fig. 4 Statistics of photovoltaic parameters for a batch of 10 devices before and after the encapsulation process (after stabilization of the cells). Boxes present the standard deviation and line bars indicate the maximum and minimum values.

To obtain stabilized cell performance, the results shown in Fig. 4 are for cells after *ca.* 7 days of their fabrication (or HTE treatment) and encapsulation process. The average results showed a slight improvement of  $V_{oc}$ , FF and PCE; and a minor decrease in  $J_{sc}$ . However, the standard deviation of the parameters after encapsulation has increased, which was assigned to the recrystallization of the perovskite during the heating step of the sealing process. The  $V_{oc}$  improved from  $0.74 \pm 0.02$  V to  $0.76 \pm 0.04$  V, the  $J_{sc}$  decreased from  $18.61 \pm 1.17$  mA cm<sup>-2</sup> to  $18.29 \pm 2.10$  mA cm<sup>-2</sup>, the FF improved from  $0.57 \pm 0.05$  to  $0.59 \pm 0.05$ , and finally PCE improved from  $7.82 \pm 0.79\%$  to  $8.21 \pm 1.49\%$ . In general, the performance of the HTM-free PSC improves during several days after their fabrication date.<sup>16</sup> Therefore, the overall improvement of the cells after encapsulation may be due to the combination of perovskite recrystallization during the sealing process, and common stabilization improvements of the devices.

### Hermeticity

The hermeticity of the encapsulated packages was measured according to the A2 method of the MIL-STD-883 standard. Two batches of encapsulated devices were used to perform the hermeticity test; (i) optimized laser-assisted glass frit, and (ii) thermoplastic. Fig. 5 compares the equivalent air leak rate ( $L$ ) for the optimized laser-assisted glass frit sealed devices to devices sealed with Surlyn thermoplastic. The Surlyn sealed sample displayed leak rates higher than the rejection limit and hence it was considered as non-hermetic. Other authors have reported the non-hermeticity behavior of Surlyn for PSC application;<sup>21,22</sup> however, to the best of our knowledge, this is the first report on its leak rate. In contrast, the developed laser-assisted glass frit sealing is hermetic. As shown in Fig. S7 (ESI<sup>†</sup>) there are no pin-holes in the scanning electron microscope (SEM) image of the sealing, which is the characteristic of high sealing quality that agrees with the results of the hermeticity test.

### Long-term stability tests

HTM-free devices similar to the present study display 1000 h stability under illumination without encapsulation.<sup>16</sup> Therefore,

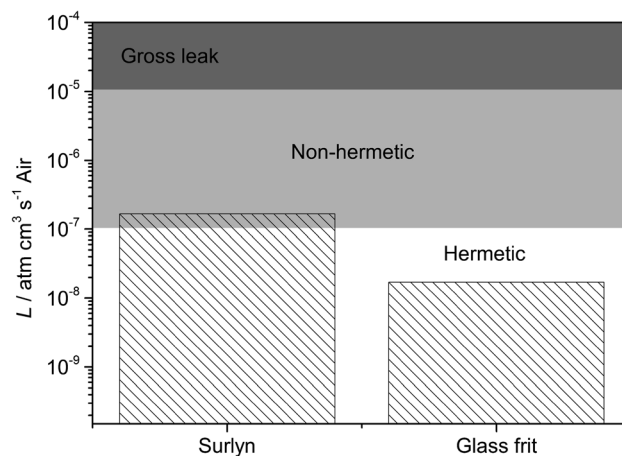


Fig. 5 Leak rates for encapsulated devices of cavity size  $2 \times 2.5$  cm<sup>2</sup>, sealed with glass frit vs. Surlyn.

the stability of the encapsulated devices of this structure was investigated under industry standard tests and harsh humidity conditions. The long-term stability analysis was divided into two groups of experiments: (i) climatic tests: stability of the hermetic encapsulation according to the IEC61646 standard and (ii) humid air feeding exposure: effect of humidity on hermetic and non-hermetic encapsulation.

Climatic tests of 70 thermal cycles and 50 h damp heat according to IEC61646 standard were performed on hermetically laser-sealed devices. As shown in Fig. 6 the IEC standard tests had minimal effect on the hermetically sealed devices. Since the encapsulation is hermetic, there should be no humidity related effects on the cells during these tests. While the temperature during the damp heat test is set to 85 °C, the temperature change from 85 °C to -40 °C of the thermal cycle caused slight decrease in the PCE of the devices. This could be due to the CTE mismatch between components of the device (TiO<sub>2</sub>, ZrO<sub>2</sub> and carbon), which can cause displacement of the perovskite absorber in the scaffold and therefore grain boundary recombination. The CTE mismatch effect during the

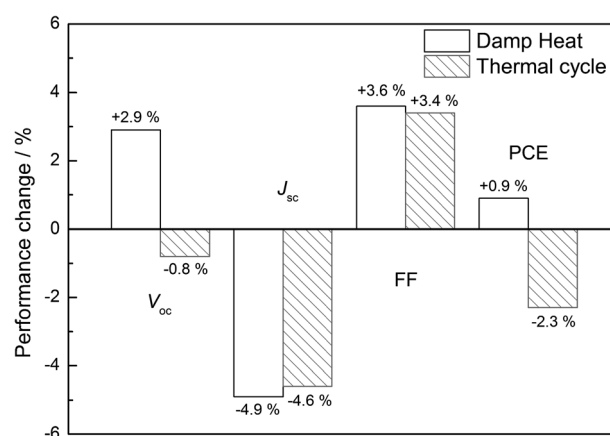


Fig. 6 Changes in the photovoltaic parameters of the hermetically encapsulated PSCs after thermal cycle and damp heat tests.

thermal cycle test has also been reported by other researchers.<sup>22</sup> The climatic test results showed that the encapsulation method is effective for elevated humidity and temperature cycling conditions.

The effect of humidity on encapsulated devices with three hermeticity levels of “no sealing”, “non-hermetic sealing” and “hermetic sealing” was investigated through humid air ( $80 \pm 5\%$  RH) feeding exposure of the devices for 500 h. The humid air feeding procedure ensures the forced entry of humidity to the cavity of encapsulated devices under study. As shown in Fig. 7a the performance of the “no sealing” devices rapidly dropped during the first hours of the humid air feeding test, while “non-hermetic sealing” cells showed losses after 50 h, and finally “hermetic sealing” PSCs retained their performance for 500 h. Fig. 7b shows the 500 h history of the normalized photovoltaic parameters for a “hermetic sealing” device.

As shown in the photograph of Fig. S8 (ESI<sup>†</sup>), after 40 h of aging the dark black colored perovskite absorber of “no sealing” cells changed to a yellowish color. The “non-hermetic sealing” cells showed a black to grey color change after 135 h of aging. The X-Ray Diffraction (XRD) of the “no sealing” sample indicates a strong  $\text{PbI}_2$  peak, while the spectra for the “non-hermetic” device are quite similar to those of the fresh reference device – Fig. S9 (ESI<sup>†</sup>). The incident photon-to-electron conversion efficiency for the “non-hermetic” device shows a decrease of photocurrent quantum yield in the spectral region from 350 to 800 nm, which is the indication of the partial decomposition of the perovskite to  $\text{PbI}_2$ <sup>29,30</sup> (Fig S10a<sup>†</sup>). Furthermore, the grey colored perovskite and lead iodide mixture of the “non-hermetic” sample shows a higher reflectance value compared to the pure black colored perovskite – Fig. S10b.<sup>†</sup> As mentioned before, the “bump” effect of the  $J$ - $V$  curve of fresh devices can be corrected through HTE treatment. Therefore, if a device is encapsulated without HTE treatment, the “bump” effect on the  $J$ - $V$  curve can be corrected only if the sealing is “non-hermetic”. As shown in Fig. S11 (ESI<sup>†</sup>), the humid air feeding affects the  $J$ - $V$  curve of the “non-hermetic” cell after 21 h of the stability test and gradually lowers the performance of the cell. In contrast, there are no changes in the  $J$ - $V$  curves of the hermetically sealed device during the 500 h stability test.

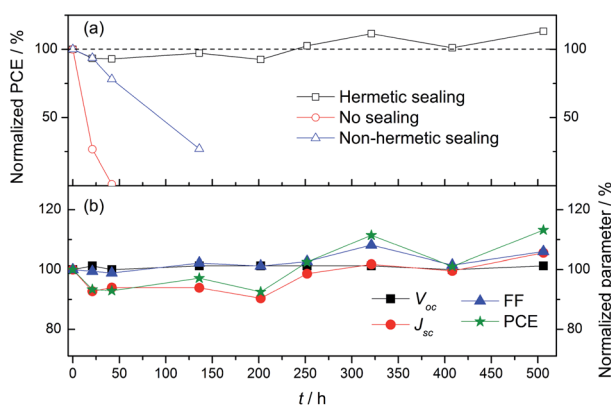


Fig. 7 Humidity aging for 500 h of (a) hermetic, non-hermetic and no sealing devices; (b) photovoltaic parameters for a hermetically laser-assisted sealed PSC.

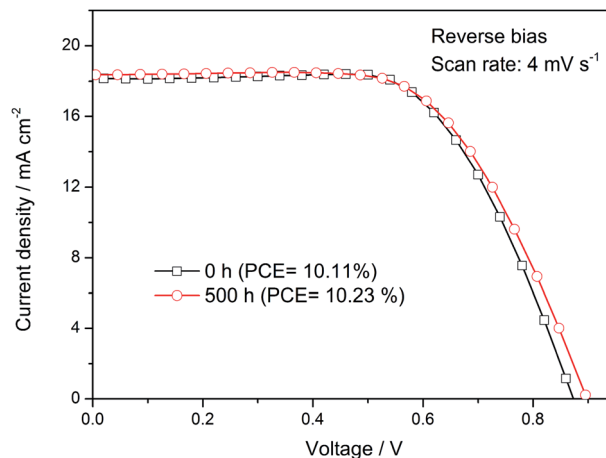


Fig. 8  $J$ - $V$  curves of a hermetically sealed PSC, before and after 500 h humidity aging test.

Regardless of HTE treatment before encapsulation, the performance of the cell should remain unchanged during the humidity stability test. However, the HTE treatment before sealing not only boosts the performance of the devices but also results in hysteresis-free devices – Fig. S12 (ESI<sup>†</sup>). Fig. 8 shows current *vs.* applied potential curves of a HTE treated hermetically sealed device before and after the humidity stability test.

### Large area device

The scale-up potential of the developed encapsulation method was shown by increasing the size of the devices from an internal cavity area of  $2 \times 2.5 \text{ cm}^2$  to  $4 \times 4 \text{ cm}^2$ . Increasing the active area of the devices commonly results in PCE reduction due to the sheet resistance of the electrodes (FTO and carbon back contact). As shown in Fig. S13<sup>†</sup> the performance of the large area device remained unchanged after the encapsulation process, which confirms that the encapsulation is scalable.

### HTM-based device

Finally, the optimal encapsulation conditions (*ca.*  $T = 100 \text{ }^\circ\text{C}$  and  $t = 35 \text{ min}$ ) were applied to encapsulate HTM-based PSCs. Device structures  $\text{meso-TiO}_2/\text{Cs}_{0.10}\text{FA}_{0.90}\text{Pb}(\text{I}_{0.83}\text{Br}_{0.17})_3/\text{HTM}/\text{Au}$  with two HTM materials PTAA and CuSCN were selected due to better thermal resistance. Despite the short thermal exposure time at  $100 \text{ }^\circ\text{C} - 35 \text{ min}$ , the performance of the devices drastically dropped after the encapsulation – Fig. S14.<sup>†</sup> Since the annealing temperature of the perovskite absorber ( $\text{Cs}_{0.10}\text{FA}_{0.90}\text{Pb}(\text{I}_{0.83}\text{Br}_{0.17})_3$ ) is  $100 \text{ }^\circ\text{C}$ , the performance loss of the HTM-based PSCs are due to the thermal instability of HTM layers at  $100 \text{ }^\circ\text{C}$ . As other authors reported good thermal stability for HTMs such as PTAA,<sup>8</sup> CuSCN<sup>10</sup> and CuPc<sup>11</sup> at  $85 \text{ }^\circ\text{C}$ , the future work is to lower the encapsulation process temperature to  $<85 \text{ }^\circ\text{C}$ .

## Conclusions

In conclusion, this study showed that hermetic encapsulation is critical for achieving long-term stability in PSCs. Although there

are other reports on long-term stable encapsulated PSCs, to the best of our knowledge, this work is the first report on an encapsulation method capable of passing hermeticity requirements of the pertinent PV standard tests. The developed glass frit encapsulation was optimized for not damaging the performance of the cells during sealing while achieving the highest hermeticity level. The hermetic sealing avoids both penetration of humidity into the cell and leakage of Pb. Moreover, the glass frit encapsulation process is compatible with PSC fabrication and does not require additional current collectors for charge extraction. The advanced encapsulation method uses a narrow 1–4 mm sealing line and the charge extraction is *via* the TCO of the substrate. Finally, from an industrialization point of view, the glass frit deposition is through screen-printing and hence scalable.

The hermetically encapsulated HTM-free PSC devices showed no significant performance losses after the thermal cycle and damp heat test according to IEC61646. Furthermore, the 500 h humid air feeding test indicated no performance change for hermetic devices, while non-hermetic devices showed degradation after the initial 50 h of the test, confirming the importance of the hermeticity level of encapsulation. Finally, the performance of all encapsulated PSCs of the present work remained stable until the present day (more than 15 months – Fig. S15†). Although HTM-free devices are promising candidates for the industrialization of perovskite solar cells, their relatively low PCE might be a drawback. In contrast, HTM-based (*e.g.* spiro-OMeTAD) devices with superior PCE are not yet ready to meet the thermal requirements of standard tests (–40 °C to 85 °C). When HTM-based devices reach that milestone, a hermetic encapsulation similar to the present work at process temperatures lower than 85 °C would guarantee the successful commercialization of a highly efficient and stable PSC.

## Conflicts of interest

There are no conflicts to declare.

## Acknowledgements

The authors would like to thank R. Madureira for preparing the scheme of the device, and Dr M. Starykevich for assistance with XRD studies. S. Emami is grateful to the Portuguese Foundation for Science and Technology (FCT) for his PhD grant (reference: SFRH/BD/119402/2016). The authors acknowledge the European Commission through the Seventh Framework Program, the Specific Program “Ideas” of the European Research Council for research and technological development as part of an Advanced Grant under Grant Agreement No. 321315 (BI-DSC). This work was partially supported by the European Union’s Horizon 2020 Programme, through an FET open research and innovation action under grant agreement no. 687008. The authors also acknowledge the projects: (i) POCI-01-0145-FEDER-006939, funded by the Regional Development Fund (ERDF), through COMPETE2020 – Programa POCI and by national funds through FCT and (ii) NORTE-01-0145-FEDER-000005 –

LEPABE-2-ECO-INNOVATION, supported by North Portugal Regional Operational Programme (Norte 2020), under the Portugal 2020 Partnership Agreement, through the ERDF. This work was financially supported by the project UID/EQU/00511/2019 – Laboratory for Process Engineering, Environment, Biotechnology and Energy – LEPABE funded by national funds through FCT/MCTES (PIDDAC). Part of this work was also performed under the projects (i) “SunStorage – harvesting and storage of solar energy”, with reference POCI-01-0145-FEDER-016387, and (ii) Sunflow – Solar energy storage into redox flow batteries” with reference PTDC/EQU-EQU/30510/2017 – POCI-01-0145-FEDER-030510, funded by (ERDF), through COMPETE 2020 – (OPCI), and by national funds, through FCT.

## References

- 1 A. Kojima, K. Teshima, Y. Shirai and T. Miyasaka, *J. Am. Chem. Soc.*, 2009, **131**, 6050–6051.
- 2 NREL, <https://www.nrel.gov/pv/assets/pdfs/best-research-cell-efficiencies.pdf>, accessed on: 2019/02/15, 2019.
- 3 D. Wang, M. Wright, N. K. Elumalai and A. Uddin, *Sol. Energy Mater. Sol. Cells*, 2016, **147**, 255–275.
- 4 IEC61646, International Electrotechnical Commission, 2008.
- 5 K. Qin, B. Dong and S. Wang, *J. Energy Chem.*, 2019, **33**, 90–99.
- 6 A. Dualeh, N. Tétreault, T. Moehl, P. Gao, M. K. Nazeeruddin and M. Grätzel, *Adv. Funct. Mater.*, 2014, **24**, 3250–3258.
- 7 G. E. Eperon, S. D. Stranks, C. Menelaou, M. B. Johnston, L. M. Herz and H. J. Snaith, *Energy Environ. Sci.*, 2014, **7**, 982–988.
- 8 M. Saliba, T. Matsui, J.-Y. Seo, K. Domanski, J.-P. Correa-Baena, M. K. Nazeeruddin, S. M. Zakeeruddin, W. Tress, A. Abate, A. Hagfeldt and M. Grätzel, *Energy Environ. Sci.*, 2016, **9**, 1989–1997.
- 9 K. Domanski, J.-P. Correa-Baena, N. Mine, M. K. Nazeeruddin, A. Abate, M. Saliba, W. Tress, A. Hagfeldt and M. Grätzel, *ACS Nano*, 2016, **10**, 6306–6314.
- 10 N. Arora, M. I. Dar, A. Hinderhofer, N. Pellet, F. Schreiber, S. M. Zakeeruddin and M. Grätzel, *Science*, 2017, **358**, 768–771.
- 11 Y. C. Kim, T. Y. Yang, N. J. Jeon, J. Im, S. Jang, T. J. Shin, H. W. Shin, S. Kim, E. Lee, S. Kim, J. H. Noh, S. I. Seok and J. Seo, *Energy Environ. Sci.*, 2017, **10**, 2109–2116.
- 12 I. Mesquita, L. Andrade and A. Mendes, *ChemSusChem*, 2019, **12**, 2186–2194.
- 13 G. Xing, N. Mathews, S. Sun, S. S. Lim, Y. M. Lam, M. Grätzel, S. Mhaisalkar and T. C. Sum, *Science*, 2013, **342**, 344–347.
- 14 L. Etgar, P. Gao, Z. Xue, Q. Peng, A. K. Chandiran, B. Liu, M. K. Nazeeruddin and M. Grätzel, *J. Am. Chem. Soc.*, 2012, **134**, 17396–17399.
- 15 C. Tian, A. Mei, S. Zhang, H. Tian, S. Liu, F. Qin, Y. Xiong, Y. Rong, Y. Hu, Y. Zhou, S. Xie and H. Han, *Nano Energy*, 2018, **53**, 160–167.
- 16 A. Mei, X. Li, L. Liu, Z. Ku, T. Liu, Y. Rong, M. Xu, M. Hu, J. Chen, Y. Yang, M. Grätzel and H. Han, *Science*, 2014, **345**, 295–298.

- 17 S. G. Hashmi, D. Martineau, M. I. Dar, T. T. T. Myllymaki, T. Sarikka, V. Ulla, S. M. Zakeeruddin and M. Grätzel, *J. Mater. Chem. A*, 2017, **5**, 12060–12067.
- 18 MIL-STD-883H, United States Department of Defense, 2010.
- 19 S. Emami, J. Martins, L. Andrade, J. Mendes and A. Mendes, *Opt. Lasers Eng.*, 2017, **96**, 107–116.
- 20 L. Y. Il, J. N. Joong, K. B. Jun, S. Hyunjeong, Y. Tae-Youl, S. S. Il, S. Jangwon and I. S. Gap, *Adv. Energy Mater.*, 2018, **8**, 1701928.
- 21 F. Matteocci, L. Cinà, E. Lamanna, S. Cacovich, G. Divitini, P. A. Midgley, C. Ducati and A. Di Carlo, *Nano Energy*, 2016, **30**, 162–172.
- 22 R. Cheacharoen, N. Rolston, D. Harwood, K. A. Bush, R. H. Dauskardt and M. D. McGehee, *Energy Environ. Sci.*, 2018, **11**, 144–150.
- 23 T. Leijtens, G. E. Eperon, S. Pathak, A. Abate, M. M. Lee and H. J. Snaith, *Nat. Commun.*, 2013, **4**, 2885.
- 24 Q. Dong, F. Liu, M. K. Wong, H. W. Tam, A. B. Djurišić, A. Ng, C. Surya, W. K. Chan and A. M. C. Ng, *ChemSusChem*, 2016, **9**, 2597–2603.
- 25 R. Cheacharoen, C. C. Boyd, G. F. Burkhard, T. Leijtens, J. A. Raiford, K. A. Bush, S. F. Bent and M. D. McGehee, *Sustainable Energy Fuels*, 2018, **2**, 2398–2406.
- 26 F. Ribeiro, J. Maçaira, R. Cruz, J. Gabriel, L. Andrade and A. Mendes, *Sol. Energy Mater. Sol. Cells*, 2012, **96**, 43–49.
- 27 S. Emami, J. Martins, R. Madureira, D. Hernandez, G. Bernardo, J. Mendes and A. Mendes, *J. Phys. D: Appl. Phys.*, 2019, **52**, 074005.
- 28 T. J. Lu and N. A. Fleck, *Acta Mater.*, 1998, **46**, 4755–4768.
- 29 A. M. A. Leguy, Y. Hu, M. Campoy-Quiles, M. I. Alonso, O. J. Weber, P. Azarhoosh, M. van Schilfgaarde, M. T. Weller, T. Bein, J. Nelson, P. Docampo and P. R. F. Barnes, *Chem. Mater.*, 2015, **27**, 3397–3407.
- 30 J. Yang, B. D. Siempelkamp, D. Liu and T. L. Kelly, *ACS Nano*, 2015, **9**, 1955–1963.